UNIVERSITÀ DEGLI STUDI DI PADOVA

Dipartimento di Fisica e Astronomia "Galileo Galilei"

Corso di Laurea Triennale in Fisica

Tesi di Laurea

Exploring the Pulse Shape Discrimination capabilities of the ΔE silicon detectors of the EUCLIDES array

Relatore

Dr. Alain Goasduff

Correlatori

Dr. Marco Siciliano

Dr. Daniele Mengoni

Laureando

Giovanni Sighinolfi

Anno Accademico 2017/2018

Contents

1 Introduction

The GALILEO project at Laboratori Nazionali di Legnaro (LNL) aims to explore the nuclear structure at extreme conditions, such as exotic excited states produced at very low cross section. The final configuration of the GALILEO array is a 4π high-efficiency ball, made up of germanium detectors. In its current implementation, only the backward hemisphere and a 90^o ring are used, as shown in Fig. 1(a). In order to improve its selectivity, different ancillary devices, which can help to select processes with much higher resolution than simple γ-detection, are coupled to it: Neutron Wall (which will also be mentioned in this work), NEDA (NEutron Detector Array) and EUCLIDES are some examples. The EUCLIDES array, pictured in Fig. 1(b), is a silicon ball, with a diameter close to 13 cm, which constitutes a light charged-particles detector. The complete array is made of 55 ΔE-E pentagonal and hexagonal telescopes, which provide a solid angle coverage close to 4π. The silicon thickness is $\sim$130 μm and $\sim$1000 μm for ΔE and E layers respectively and the surface of each telescope is $\sim$10 cm^2.

Because of the kinematic enlargement of the solid angle in the center of mass frame of reference for a typical fusion-evaporation reaction (v/c$\approx$5%), the most forward positioned telescopes have to deal with higher counting rates with respect to the others; thus, 5 of them are segmented in 4 equal parts, with individual electronic processing circuits, to reduce the probability of pile-up and increase the counting rate capabilities.

The first advantage of the coupling of GALILEO and EUCLIDES array is that, since in a fusion-evaporation process various species are produced in different evaporation channels, simultaneous detection of evapored light particles (such as protons, deuterons, α, etc.) and emitted γ rays can lead to the maximum selectivity. Another considerable benefit is to have the possibility to reconstruct event-by-event the trajectory of the recoiling nuclei, in order to reduce the Doppler broadening of peaks in the recorded γ-ray spectra.

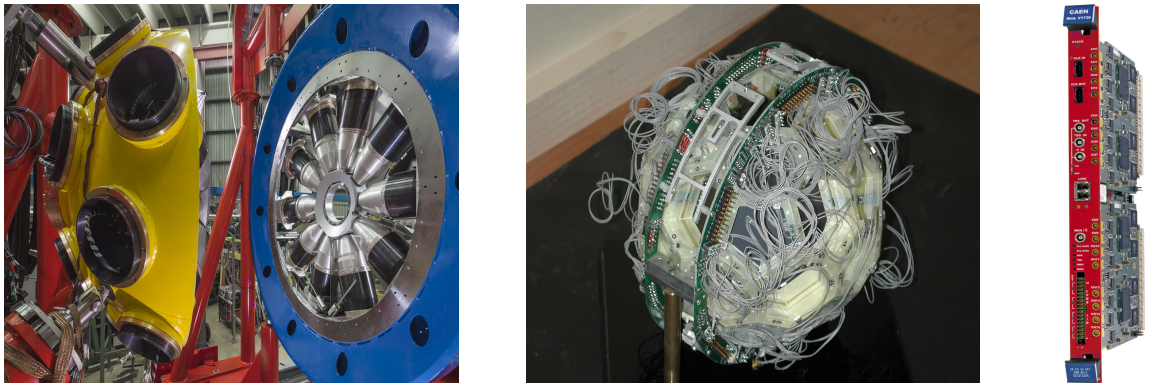

(a) (b) (c)

Figure 1: The current configuration of the GALILEO array (a), the light charged particles detector EUCLIDES (b) and the CAEN V1730B 500MS/s digitizer (c)

EUCLIDES has already been used successfully in the past years at LNL in different GALILEO experiments and it will certainly be an important tool for the forthcoming ones using radioactive ions beams delivered in the near future by the SPES facility.

In December 2017, 3 E-ΔE segments of one forward segmented telescope were connected to a CAEN V1730B (Fig. 1(c)), which is a 1-unit wide VME module housing 16 channels

14-bit 500 MS/s Flash ADC Waveform Digitizer, therefore it is able to take a sample every 2 ns, for 16 different channels, at the same time. The configuration of the digitizer in terms of trigger channels, trigger levels, polarity of the input channels etc. are set using a text file read by the CAEN software WaveDump. The traces from each active channels are dumped in separated binary files as soon as one of the active channel is triggering.

The aim of the implementation of the new digitizer in the read-out chain of EUCLIDES is to have the possibility to distinguish between α particles and protons stopping in the ΔE layer. Depending on the kinematics of the reaction and the thickness of the absorber layers, used to prevent the elastic scattering of the beam from reaching the detectors, those events stopping in the ΔE can represent more than 50% of the detected particles, thus it would be an important step forward to have the possibility to recover such events. In order to reach the maximum particle detection efficiency and selectivity in the light charged particle-γ-rays in fusion-evaporation reaction, new methods of particles discrimination for the EUCLIDES array have been investigated.

The purpose of this work is, therefore, the pulse shape analysis of the waveforms obtained from the 3 telescopes connected to the digitizer. After a preliminar study of the performances of the CAEN V1730B module, the response of the described setup to an in-beam experiment will be explored. This will include a detailed study of all the main information obtainable from the analysis of the resulting traces, in particular the energy and the timing, which are the basic elements to attain an identification of the particles stopped in the ΔE layer of the telescope.

2 Performances of the CAEN V1730B

In order to better understand the characteristics of the CAEN V1730B, a comparison with a CAEN DT5720 12-bit 250 MS/s digitizer was made. To achieve this, a BNC mod. 9010 programmable pulse generator was used to form a ∼1 V exponentially decaying signal, which was then copied and delayed by 16.0±0.2 ns (excluding the length of the cables) by the CAEN mod. N108A dual delay. Both the original and the delayed signals were then sampled by the considered digitizer and dumped in a file through WaveDump, after a check of the correct functioning of the setup, always using the CAEN software (see Fig. 2).

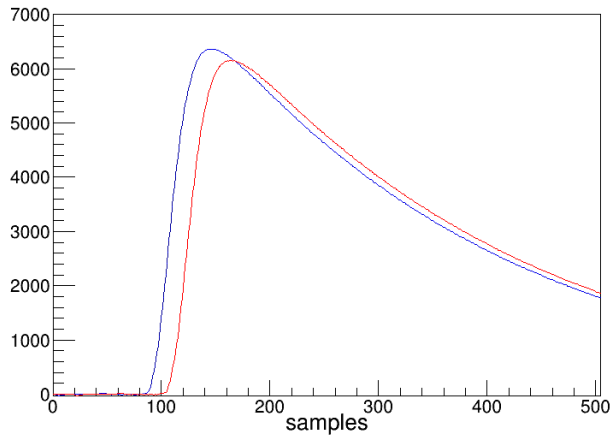

Figure 2: Digitized pulser signals after baseline substraction. The orginal signal (blue) and delayed one (red) are both sampled at 500 MS/s using the V1730 digitizer

The files so created were finally analysed through a C++ program, specially written for the analysis of the dumped signals, which converts them to ROOT files and form a Tree containing the following Branches:

- **Channel**: returns the channel number;
- **EventCounter**: returns the event number;
- **TimeStamp**: returns the timetag of the sample;
- **TraceItem**: returns the trace element;
- **IntegratedSignal**: returns the area under the trace;
- **Baseline**: sets the integral under which a signal is considered baseline;
- **LeadingEdge**: sets a threshold, passed which the signal is considered of interest: in this case, the CFD is calculated;
- **ZeroCrossing**: returns the first positive sample of the CFD trace;
- **CFD**: returns the point in which the CFD trace overcomes the zero (expressed in samples);

Later, other important features will be inserted in the analysis, such as the energy or the polarity, which are not relevant at this point.

2.1 Constant Fraction Discriminator

The Constant Fraction Discriminator is a technique to modify the original signal, in order to get a preciser evaluation of the timing. As shown in Fig. 3, the wave is reduced by a certain value named fraction, inverted, delayed, and finally summed to the original one. Thus, the performance of such technique depend on two different parameters: the fraction and the delay.

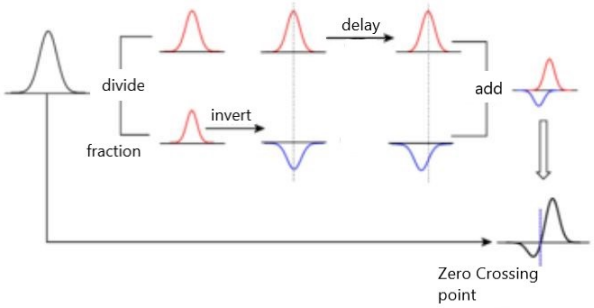

Figure 3: Representation of the operations needed to get a CFD trace: the wave is reduced by a certain value named fraction, inverted, delayed, and finally summed to the original one

To achieve this, the program selects a signal that passes the Leading Edge, generates its CFD trace and finds the Zero Crossing point. The CFD value is finally calculated by doing a quadratic or linear fit of four points around the Zero Crossing sample or a simple interpolation of the Zero Crossing with the previous sample. In every case, the CFD value is the intersection between the curve and the baseline: the chosen esteem is the precisest positive one (so the one obtained through the quadratic fit, preferably).

2.2 DT5720 analysis

At first, the CAEN DT5720 digitizer was used in the read-out chain and the CFD values of its traces were evaluated. The quality of the CFD implementation depends on the choice of the parameters used, therefore an accurate investigation has been performed through the trial of many different combinations of fraction and delay, looking for the ones minimizing the width of the time difference distribution obtained using the CFD of the two waveforms. The resulting plot is reported in Fig. 4(a): since there clearly is an entire region of minimum, at this order of precision, another optimization with smaller parameters step was held in that zone, leading to the selection of

$$fraction = 42, \quad delay = 29$$

(which means that the original trace is reduced by the 42% and delayed by 29 samples). The gaussian fit of the CFD difference obtained with those values is also reported, in Fig. 4(b): firstly, we notice that the mean is higher than the set delay and it can be explained by the length of the cables which introduce an additional delay between the signals; secondly, the time resolution can be evaluated as

$$FWHM = \sqrt{8 \cdot ln(2)} \cdot \sigma \simeq 2.355 \cdot \sigma = 61.3 \pm 0.2\, ps.$$

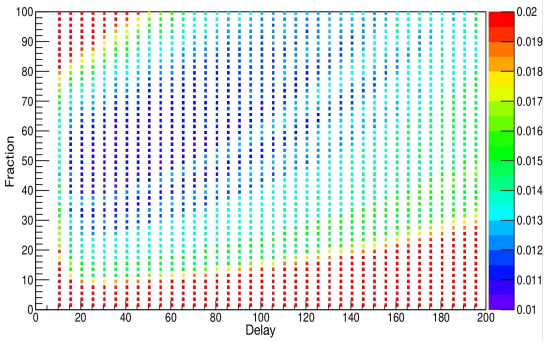

(a) Plot of the values of σ of the gaussian fit of the CFD difference for given fraction (measured in percentage of the original wave) and delay (in samples)

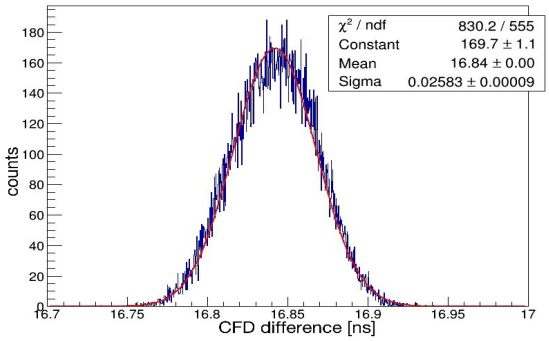

(b) Gaussian fit of the CFD difference between two equal signals, delayed by 16 ns and sampled by the 250 MS/s digitizer

Figure 4: Search for the optimal CFD parameters and the related gaussian fit, using the CAEN DT5720 module

2.3 V1730B analysis

Since the CAEN V1730B is a 500MS/s digitizer, while the DT5720 is a 250 MS/s, it was assumed, without doing the same test utilized for the construction of Fig. 4(a), that a good set of CFD parameters, would have been

$$fraction = 42, \quad delay = 58.$$

The result of the analysis carried out through this device is shown in Fig. 5. The mean, in this case, is even higher than the previous one (Fig. 4(b)), because it was necessary to add a $\sim$1 ns cable in the read-out chain, but the time resolution is more precise, also considering that a detailed optimization of the parameters was not achieved (this is justified by the fact that new values needed to be found anyway when elaborating the traces of real particles), in fact:

$$FWHM = 50.3 \pm 0.2\ ps$$

which corresponds to the 82% of the previous outcome.

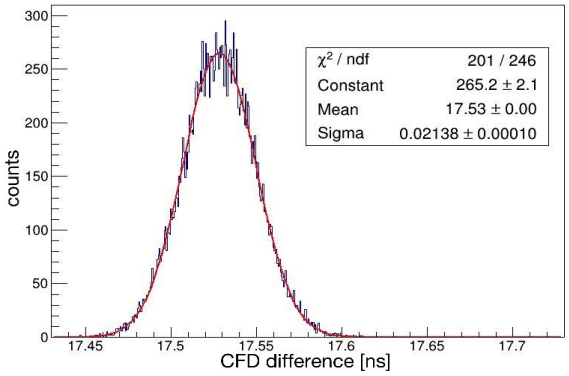

Figure 5: Gaussian fit of the CFD difference between two equal signals, delayed by 16 ns and sampled by the CAEN V1730B 500 MS/s digitizer

3 Experimental setup

In December 2017, an experiment was held at LNL, in which a 250 MeV ^{64}Zn stable beam was impinging on a $\sim$0.62 μm ^{3}He target, implanted in a W layer deposited on a thick Au backing. This target, produced with an innovative procedure, contains a density of $\sim 0.3 \cdot 10^{18}$ atoms/cm^2 of ^{3}He. Traces of ^{16}O have been inferred during the online analysis from the γ-rays spectra. For the simulations of the experiment, presented in section 5.2, this contamination of the target will be taken into account, and both the processes will be investigated.

During the experiment, the EUCLIDES array was installed in the GALILEO reaction chamber and the CAEN V1730B was used for the readout 3 segments of one of the most forward telescopes. The even channels 2, 8 and 12 were used for ΔE, while the following odd ones (so 3,9 and 13) were connected to the respective E layers. Channel 6 was connected to the OR signal of the Neutron Wall array. In order to limit the dead time that would come when triggering on Neutron Wall array (400 kHz in the present condition), this channel was chosen to be used as a slave of the telescope, i.e. the Neutron Wall channel was recorded only when it was in coincidence within a 2 μs window with a signal recorded from EUCLIDES.

An example of the obtained traces, plotted in real-time through the WaveDump software, is shown in Fig. 6. The vertical lines close to 1.25 and 1.5 μs correspond to the OR trigger coming from the Neutron Wall array. The polarity of the waves was set negative in the digitizer options and the leading edge threshold of every channel was adjusted individually for each of them. Finally a 50 Ω termination was placed on the positive output of the differential-to-single-ended conversion box for the EUCLIDES signals (the channels of the digitizer were connected to the negative ones). As expected, the amplitude of the waveforms coming from odd channels is larger than the one of even channels, since the firsts are connected to E segments, in which the energy loss is higher.

It is relevant to say that one was able to notice the presence of very low signals in different channels, that could also be positive: an accurate study on this fact will be proposed in section 4.3.

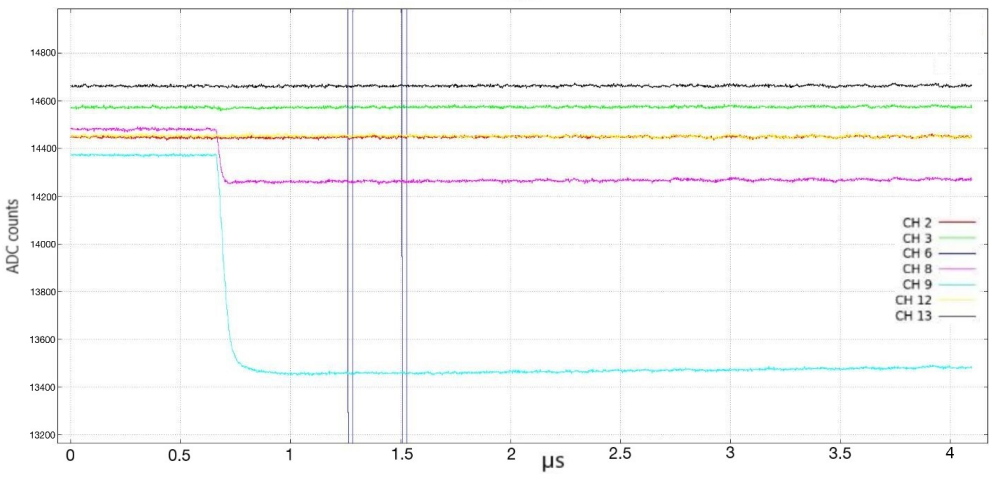

Figure 6: Example of the online experimental waveforms digitized by the CAEN V1730B module

4 Data analysis

To analyse the waveforms of the in-beam data, additional Branches were added to the Tree described in section 2:

- **Polarity**: returns the polarity of the trace;
- **TrapeItem**: returns the trapezoidal filter element;
- **Energy**: returns the energy related to the trace (in arbitrary units), evaluated basing on the trapezoidal filter;

Note also that the program used for the analysis inverts all the negative signals, in order to simplify the process of evaluation of the CFD and the trapezoidal filter.

A program was also written to merge all the ROOT files containing the information of the different channels into a single one. Doing this, it was finally possible to make comparisons and operations between, for example, a ΔE channel and the related E one.

4.1 Energy

The trapezoidal filter represents a technique for the synthesis of optimal pulse shapes for high resolution spectroscopy. It was implemented following the equations established by Jordanov et al. in [5] on all the traces overcoming a software threshold. This second threshold has been set to reduce the processing time, because the CAEN V1730B digitizes all the active channels and dumps them to disk as soon as one of them is overcoming the hardware trigger threshold. As described in Fig. 7, the parameters of interest for the constitution of the trapezoidal filter are:

- **k**: sets the length of the rise time of the trapezoid;
- **l**: represents the sum of the rise time and the flat top length, m, which should be long enough to ensure the possibility to calculate a reasonable value of the energy: in all the considered cases, this is widely guaranteed, since the program evaluates the energy as the simple mean of 20 samples around the maximum point of the flat top and the number of samples taken by the 500MS/s digitizer ensure that this condition is always satisfied;
- **k'**: sets a delay in the rise time of the trapezoid.

The choice of the best parameters has been achieved through the trial of different combinations of them, concluded with the following values:

$$k = 285\ samples, \quad l = 500\ samples, \quad k' = 5\ samples.$$

With these parameters, the trapezoidal filter has the right shape, for channel 13 in particular (see Fig. 8(b)). In general, a worsening of the flat top of the trapezoids is observable with the decreasing of the amplitude of the waveforms, since the traces become noisier. Consequently, the shapes formed for ΔE channels, in most cases, look fragmented on the flat top (see Fig. 8(d)), because they tipically record lower amplitude traces with respect to the E ones, since the energy lost by particles crossing them is also lower. This could be an issue, but, since the oscillation of the flat top was observed to be in the order of 1 unit in the arbitrary scale, we assumed that the energy extracted from the trapezoidal filter is acceptable. Other parameters were tried separately for the different channels, but with none of them a

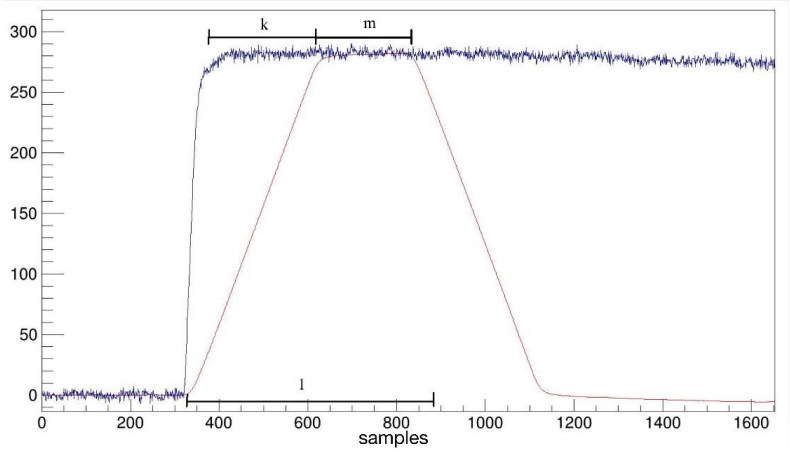

Figure 7: Example of trapezoidal filter of an experimental waveform, showing the filter parameters k (rise time), m (flat top) and l (sum of the two)

consistent improvement was observed. For channels 2 and 3, parameters resulting in well defined trapezoidal shapes were not actually found (see Fig. 8(f)). Also their waveforms present unforeseen behaviors, especially at low energies, as shown in Fig. 8(e), for example for channel 2. Basing on that, we can likely affirm that there was an issue in the electronic processing circuit of those channels.

Considering the full statistic, it was possible to form very precise E-ΔE matrices for both the channels pairs 9-8 and 13-12, visible in Fig. 9. The one of channels 3-2 is also reported: for these channels, complete structures are not formed, presenting very little statistic at low energy.

In these plots, one can clearly distinguish protons, deuterons, ^{3}He and α particles and see the punch-through of p, d and α. Also the traces of t, 2p (or its pile-up) and the coincidence of α particles and protons are slightly visible for channels 9-8 in particular, but they can not be used for further studies, with this level of statistic. Notice that the number of events of ^{3}He considerably increases at high energy: the cause of this is the elastic scattering between the beam and the target, as it will be demonstrated in section 5.1. Since it does not provide enough energy to cause the punch-through of the isotope, the event is not observable in the matrices.

The matrices in Fig. 9 allowed to calibrate the channels, even if for channel 3 only two points could be used, since the punch-through of α was not observed. The theoretical values, to compare with the ones obtainable studying the matrices, were evaluated through the Physical Calulator of LISE++, looking for the maximum energy that the identified particles can have to be stopped by a 130 μm Si layer (ΔE) or a sequence of a 130 μm and a 1000 μm Si layers (ΔE+E), in this case selecting only the energy lost in the second one. The first one corresponds to the value of the intersection between the y axis (i.e. E=0) and the extension towards it of the trace of the energy loss , while the second one corresponds to the projection on x axis of the punch-through point.

The values used for the calibration and the obtained correspondence channel-energy are summed up in table 1. Note that:

- the errors on the theoretically calculated values are esteemed as half of the precision

used for their evaluation;

- the errors on the ΔE values are set as the projection on the y axis of the width of the energy loss structures;
- the errors on the E values are evaluated as the region in which one could likely position

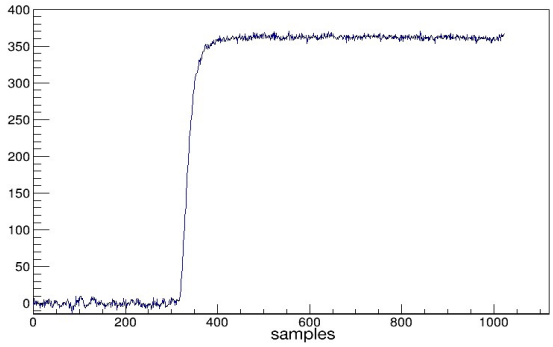

(a) Trace from channel 13 (E)

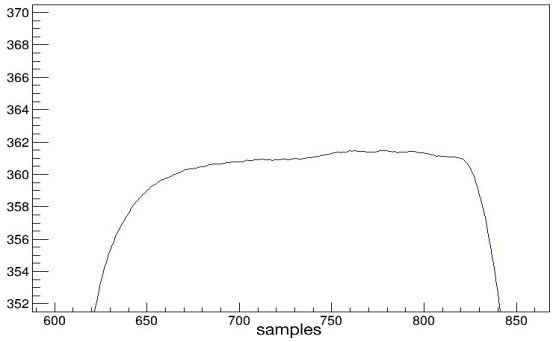

(b) Top of the trapezoidal filter of the trace reported in Fig. 8(a)

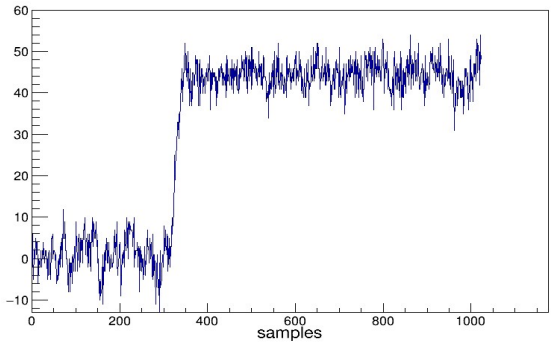

(c) Trace from channel 12 (ΔE)

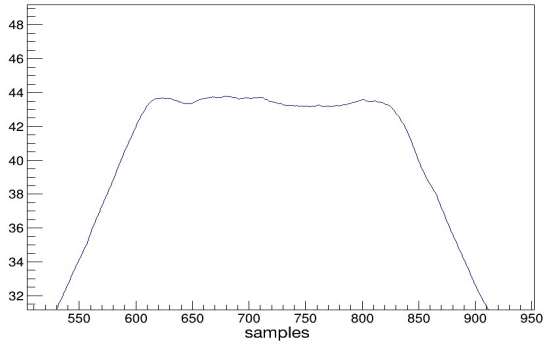

(d) Top of the trapezoidal filter of the trace reported in Fig. 8(c)

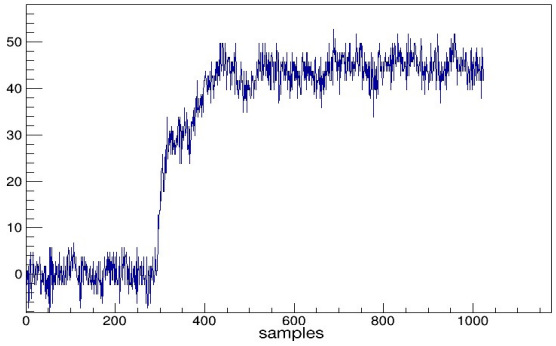

(e) Trace from channel 2 (ΔE)

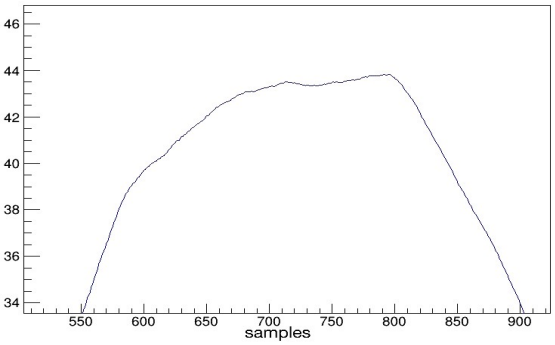

(f) Top of the trapezoidal filter of the trace reported in Fig. 8(e)

Figure 8: Example of E and ΔE waveforms and flat top of their respective trapezoidal filters

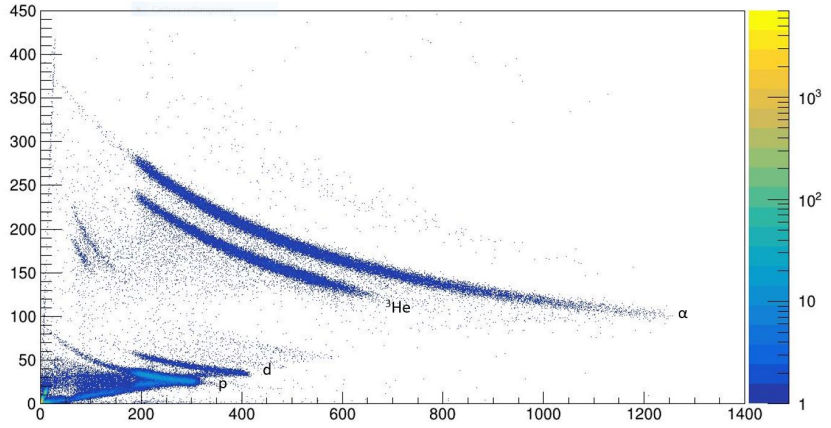

(a) E-ΔE matrix for channels 3-2

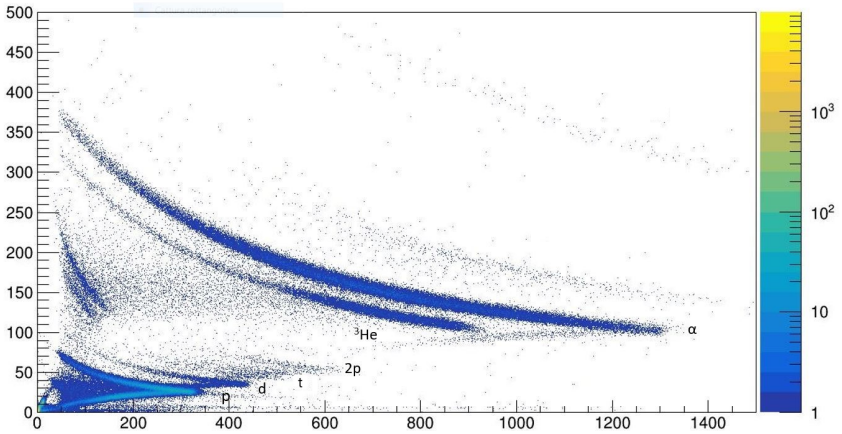

(b) E-ΔE matrix for channels 9-8

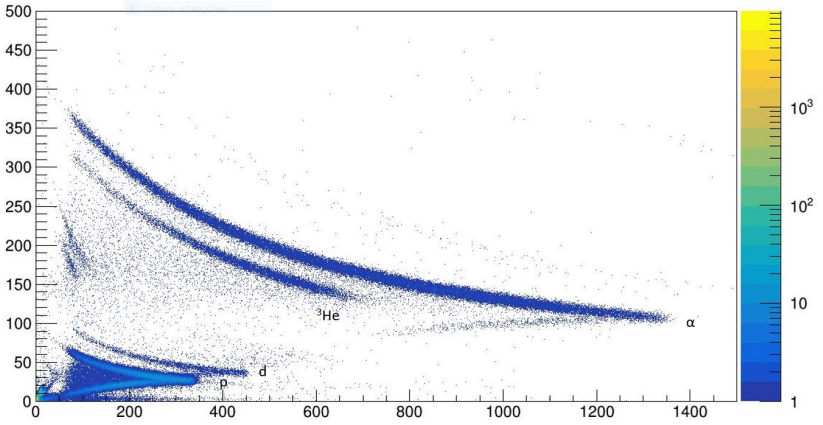

(c) E-ΔE matrix for channels 13-12

Figure 9: E-ΔE matrices for the three telescopes used during the in-beam experiment.

the punch-through point.

Table 1: Calibration points used for the linear fits

	p	d	^{3}He	α
ΔE (MeV)	3.720±0.005	4.890±0.005	13.290±0.005	14.870±0.005
ch 2	100±5	—	370±5	410±5
ch 8	105±5	140±5	390±5	435±5
ch 12	105±5	140±5	390±5	435±5
E (MeV)	12.330±0.005	16.510±0.005	—	49.240±0.005
ch 3	305±5	400±5	—	—
ch 9	320±5	425±5	—	1290±10
ch 13	330±5	440±5	—	1325±10

The parameters of the linear fit

$$ch = E \cdot p_1 + p_0$$

are finally collected in table 2. The fact that the calibration, in some cases, is different, even if the parameters used for the trapezoidal filter are always the same, is explicable because the amplitude of the waveforms depends also on the electronics of the individual channel (the high voltage in particular), so, since every segment of the telescope is connected to a separate circuit, this is perfectly admissible.

Table 2: Parameters of the linear fits for the calibration of every channel

	p_0 (ch)	p_1 (ch/MeV)	Rel. err. p_1
ch 2	-2.9±6.9	28.0±0.6	2.1 %
ch 3	25.2±24.7	22.7±1.7	7.5 %
ch 8	-4.9±5.3	29.7±0.5	1.7 %
ch 9	-4.5±6.4	26.3±0.3	1.1 %
ch 12	-4.2±5.3	29.7±0.5	1.7 %
ch 13	-2.7±6.4	26.9±0.3	1.1 %

4.2 Timing performances

The precise determination of the triggering time and time resolution, as mentioned previously, is one of the key aspects of this work. Indeed, the final goal of this study, is to investigate if a discrimination of the charged particles based on their Time of Flight is possible with the EUCLIDES array. This would represent a large gain in selectivity for the GALILEO-EUCLIDES setup in particular for the low energy particles that are stopping in the ΔE layer. Consequently, much effort has been spent in the search for the best CFD parameters, in order to achieve the best time resolution possible.

4.2.1 CFD difference between E and ΔE channels

The optimization algorithm, developed in section 2.2, was applied to the in-beam data, with the difference that, in this case, the gaussian fit was not made on the CFD difference between two signals already, but on the CFD histogram of each channel separately. This was done because there is no reason why the best CFD parameters for the ΔE waveforms should be the same as for the E ones, and viceversa.

At first, the research was made on low values of fraction and delay, since the lower they are, the sharper the CFD histogram should be. The results are shown in Fig. 10(a) and 10(b) for ΔE and E respectively. Two large areas of minimum were located and an additional research in those regions, allowed to pick the values highlighted in table 3.

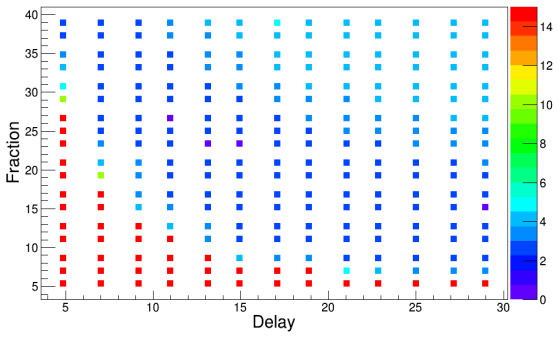

(a) Plot of the values of σ of the gaussian fit of the CFD histogram of a ΔE channel for given fraction and delay

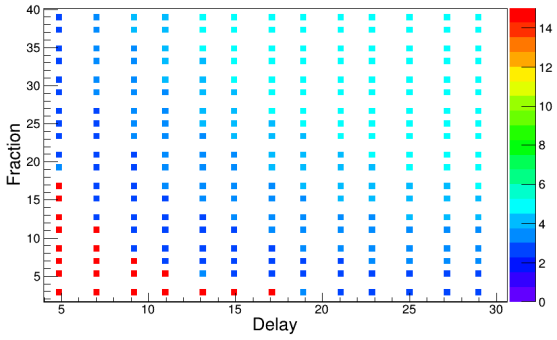

(b) Plot of the values of σ of the gaussian fit of the CFD histogram of a E channel for given fraction and delay

Figure 10: Optimization of the CFD parameters for ΔE and E layer

Table 3: CFD parameters chosen for ΔE and E channels

	fraction (% of original signal)	delay (samples)
even ch. (ΔE)	39	7
odd ch. (E)	7	15

The files were therefore elaborated setting these values. The CFD differences between the traces in E and the related traces in ΔE are reported in Fig. 11, along with their gaussian fit, from which one can deduce the time resolution by calculating the FWHM, as resumed in table 4.

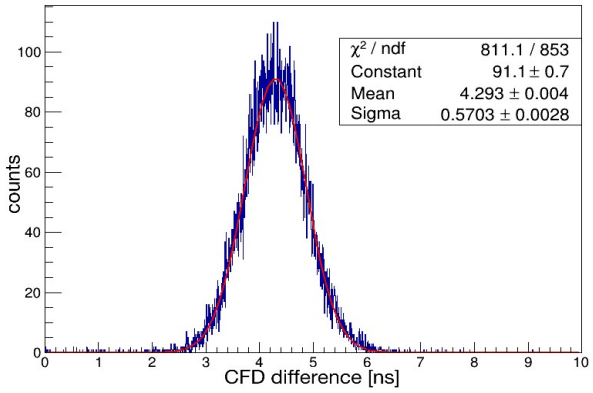

(a) Gaussian fit of the CFD difference between channels 3-2

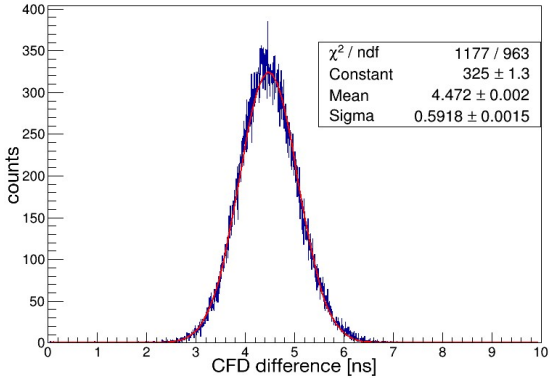

(b) Gaussian fit of the CFD difference between channels 9-8

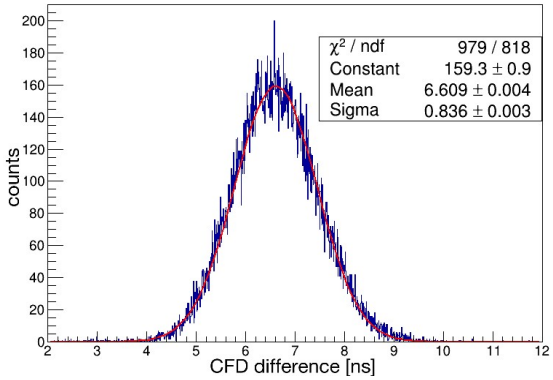

(c) Gaussian fit of the CFD difference between channels 13-12

Figure 11: Gaussian fit of the CFD difference between E and ΔE traces

Table 4: Time resolution between E and ΔE layer using CFD parameters from table 3

	ch. 3-2	ch. 9-8	ch.13-12
FWHM (ns)	1.340±0.003	1.354±0.006	1.990±0.007
Rel. err.	0.5%	0.2%	0.4%

Notice that the time resolution, which is less than 2 ns in all the cases, is very good in particular for channels 3-2. Note also that the mean of the gaussian of channels 13-12 is more than 2 ns larger than the ones of the other channels: this is due to an unwanted delay inserted in the electronic processing circuit (probably a longer cable with respect to the others) of channel 13, as verified by comparing the histograms of the CFD values of the different channels.

When checking the CFD difference for each particle type identified in the E-ΔE matrix, using graphical cuts, it was realized that the counts shown in Fig. 11 were all corresponding to ^{3}He and α at high energy (more than ∼20 MeV). This was due to the fact that the CFD

parameters reported in table 3 were not high enough to allow the low amplitude traces to overcome a threshold previously set to avoid to include the noise in the statistic. For example, the CFD traces of protons, counstructed using the parameters from table 3 are shown in Fig. 12: it is evident that none of the waveforms, of both ΔE and E channels, overcome the threshold set at -20 in arbitrary scale.

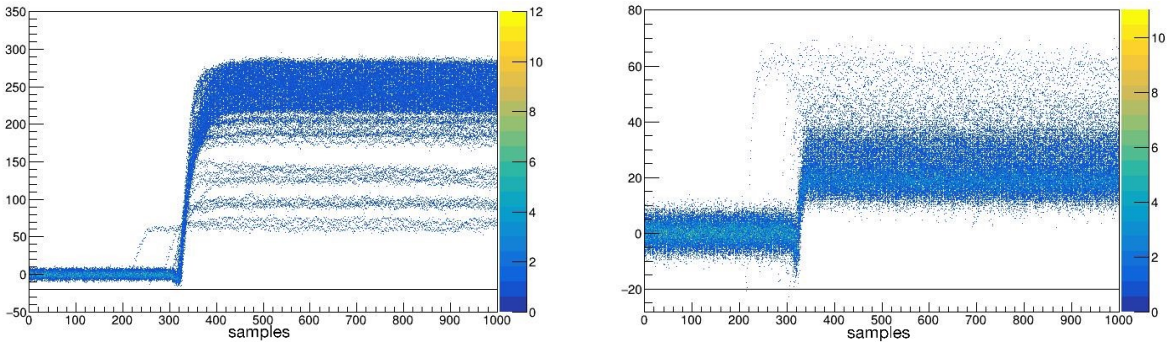

(a) CFD traces of protons in channel 9

(b) CFD traces of protons in channel 8

Figure 12: CFD traces of protons in E (a) and ΔE (b) channels, using parameters from table 3

As a consequence, it was decided to keep anyway fraction and delay values from table 3 as the best ones for high energy particles, and to search for new, higher, ones, that could be good for low energy particles as well and could therefore include the traces of protons and deuterons in particular, which were completely excluded from the previous statistic.

The search for the new parameters has been achieved as previously: a plot of the lowest values of σ of the gaussian fit in the new region of fraction and delay is reported in Fig. 13. Even if it looks like the best values are positioned in the bottom left area, attention was paid in choosing higher values of delay, because a low one would not have left the time to the CFD trace to overcome the threshold, even if the fraction would have been high enough to pass it. After some trials, the parameters from table 5 were selected, also considering the top parts of the plots shown in Fig. 10.

Table 5: CFD parameters used for ΔE and E channels (higher values)

	fraction (% of original signal)	delay (samples)
even ch. (ΔE)	42	19
odd ch. (E)	39	19

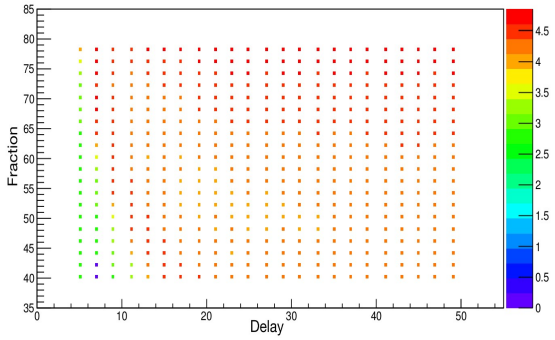

(a) Plot of the values of σ of the gaussian fit of the CFD histogram of a ΔE channel for given fraction and delay

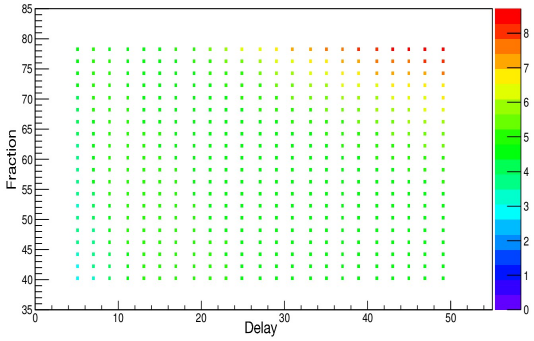

(b) Plot of the values of σ of the gaussian fit of the CFD histogram of an E channel for given fraction and delay

Figure 13: Search of the best CFD parameters for ΔE and E channels for low energy particles among high values of fraction and delay

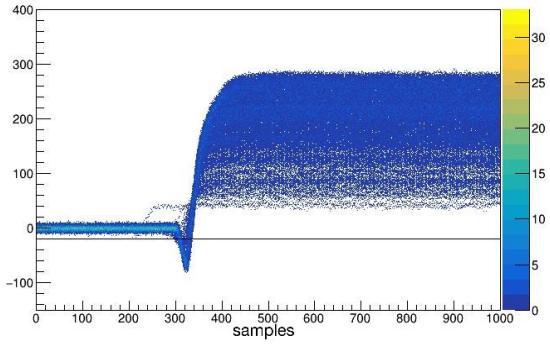

(a) CFD traces of protons in channel 9

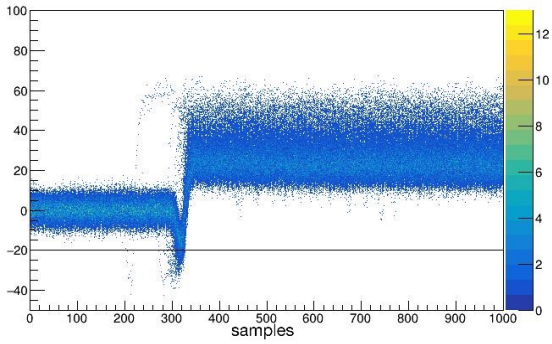

(b) CFD traces of protons in channel 8

Figure 14: CFD traces of protons in an E (a) and a ΔE (b) channels using parameters from table 5

As one can see in Fig. 14, to draw which only protons were selected, with the new CFD parameters all the E and the greatest part of the ΔE signals pass the above-mentioned threshold; therefore they were considered good for our purposes.

The CFD difference histograms have a less gaussian shape, presenting a shoulder at low time differences. An exploration of the origin of those counts was accomplished by setting some conditions: it turned out that the shoulders are due to low energy partciles, whose time resolution could not be esteemed yet. Therefore, the bumps were isolated in order to form a peak, which could then be fitted with a gaussian function. The time resolution was evaluated also in this case, and the results are reported in Fig. 15 and in table 6. For channels 9-8, a well defined histogram was obtained requesting an energy loss in the E layer lower than $\sim$16 MeV (so it includes the full statistic of p and d), while for channel 13-12, it was necessary to set an energy loss lower than 9 MeV, which only include a small part of the total p and d counts; thus, for these channels, a fit of the peak related to particles losing more than 9 MeV in the E layer is reported.

Note that for the channels 3-2, the shoulder at low time difference is not present. This is understood by looking at the E-ΔE matrix of this telescope on Fig. 9(a). The hardware

Table 6: Time resolution between E and ΔE layers with CFD parameters from table 5 for low energy particles

	FWHM (ns)	err. rel.
ch. 3-2 (no conditions)	1.681±0.009	0.5%
ch. 9-8	4.52±0.01	0.2%
ch. 13-12 (very low energy)	5.45±0.02	0.4%
ch. 13-12 (higher energy)	2.03±0.01	0.5%

triggering threshold had to be raised during the experiment which cutted a large fraction of the low energy signal on the E layer. This also explains why the time resolution of this telescope is better than the one of the two others. In fact, it is well known that the CFD determination capabilities is weaker at low energies and as this telescope was having mostly high energy signals in the E layer, the determination of the CFD on the E is intrinsically better.

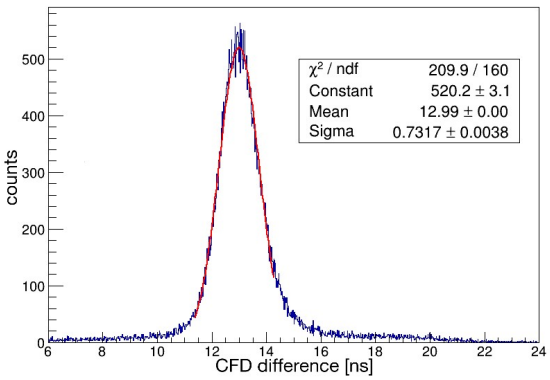

(a) CFD difference between E and ΔE traces of channels 3-2 and gaussian fit of the peak

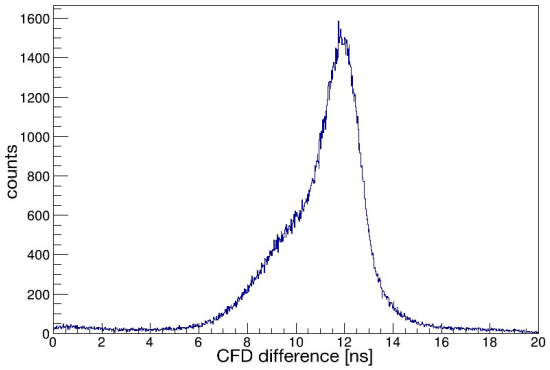

(b) CFD difference between E and ΔE traces of channels 9-8

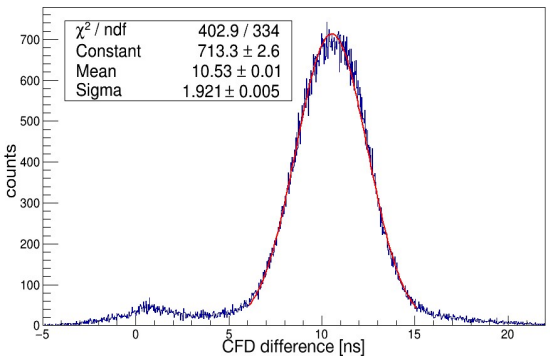

(c) Gaussian fit of the CFD difference between channels 9-8 selecting only particles with energy lower than 16 MeV

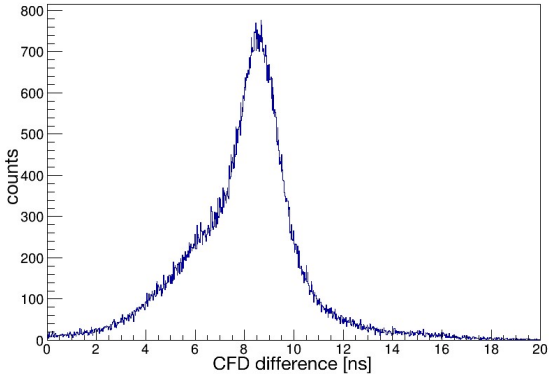

(d) CFD difference between E and ΔE traces of channels 13-12

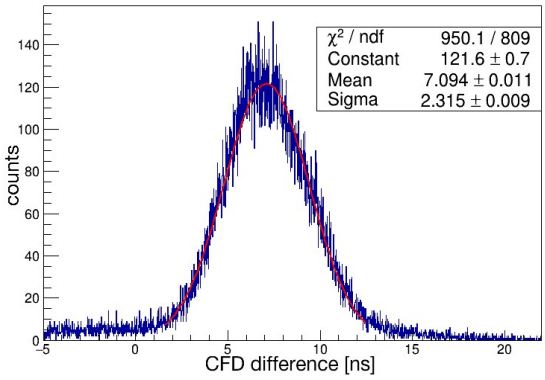

(e) Gaussian fit of the CFD difference between channels 13-12 selecting only particles with energy lower than 9 MeV

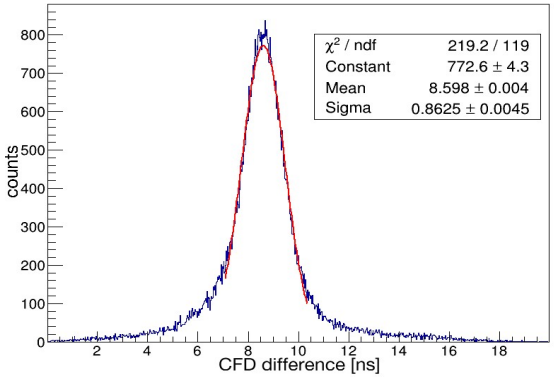

(f) Gaussian fit of the CFD difference between channels 13-12 selecting only particles with energy higher than 9 MeV

Figure 15: Histogram of the CFD difference between E and ΔE traces (parameters from table 5) and gaussian fits of the peaks obtained isolating the shoulders

4.2.2 CFD difference between NeutronWall and ΔE waveforms

As mentioned in section 3, Neutron Wall is a scintillator detector array ancillary to the GALILEO setup, which presents the advantage of being a high efficiency γ-ray detector with a fast response and quite good time resolution. Therefore, it should have a very sharp CFD trace and give a precise time resolution when coupled with another signal.

Also for the Neutron Wall OR signal, different combinations of CFD parameters were attempted, but no significant variations were observed in the output histogram. A fraction of 7 and a delay of 7 were finally chosen for its analysis.

The CFD histogram of the OR signal, shown in Fig. 16 looks different from the ones of the rest of the channels: it does not present, in fact, a single gaussian-shaped peak, but a quite large baseline arising to some peaks: the highest, sharp one, generated by the counts of γ rays, is the one of interest; the lower bump, close to 350 samples, is caused by the incidence of neutrons. Since the counts difference between the baseline and the peak is large, it was considered unnecessary to modify the CFD histogram in order to isolate the peak.

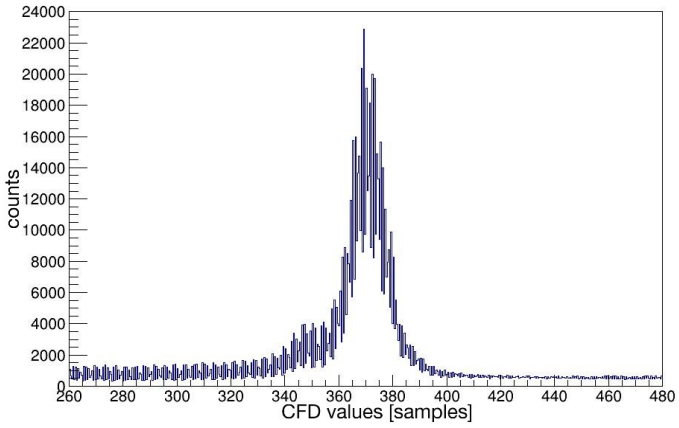

Figure 16: CFD histogram of channel 6 (Neutron Wall)

At first, the CFD of Neutron Wall was used to construct the matrix pictured in Fig. 17, where the CFD difference between channel 6 and channel 8 (representative for all the ΔE channels) is reported on the x axis and the energy lost by the particles in the first absorber layer on y axis. This plot constitutes a direct check of the correct functioning of the setup, since one can clearly see that the pulses of the beam are separated by ∼25 ns each, which is the actual time difference between the delivery of ions bunches by the Acceleratore Lineare Per Ioni (ALPI).

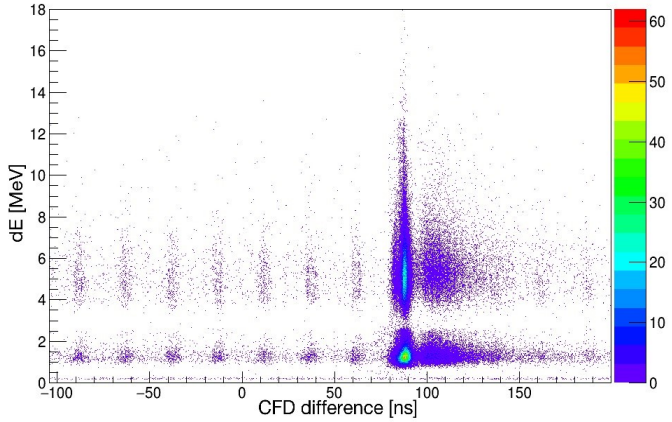

Figure 17: Matrix of the energy lost in the ΔE layer versus the CFD difference between Neutron Wall and the traces of the same ΔE layer: visualization of the beam pulses, separated by 25 ns each

Secondly, the CFD difference between the Neutron Wall and the ΔE channels (using parameters from table 6) was employed to evaluate the reachable time resolution for the particles stopping in the ΔE layer. The results are summed up in Fig. 18 and table 7, in which two cases are reported:

- without any restriction on the energy of the incident particles (see Fig. 18(a), 18(c) and 18(e));

- Setting the energy loss in the E layer equal to 0, to select only the particles stopping in the first absorber layer, and requesting $\Delta E<3.72$ MeV (which is the maximum energy that protons impinging on the telescope can have to be stopped there, as reported in table 1), in order to get the range in which it is meaningful to distinguish the particles (see Fig. 18(b) and 18(d); for channel 2, it was not possible to have a significant statistic, since it mostly includes high energy particles).

First of all, note that the CFD difference histogram presents, as expected, a high and quite sharp peak, followed by a small large bump: following the same reasoning previously described, the peak must be formed by the CFD difference with the OR signals generated by the γ rays, while the following bump comes from the difference with the traces of neutrons, which present a worse time resolution, compared to γ rays, and less statistic. This is also verified by the fact that the temporal difference between the peak and the bump is $\sim$15-16 ns: a simulation of the experiment was run using the COMPA software (see section 5.2 to better understand this procedure) to extract the Time of Flight needed by neutrons to get to the Neutron Wall (distant 51 cm from the target) and the result is reported in Fig. 19. The greatest part of neutrons require from 10 to 15 ns to get to the scintillator; considering that neutrons are also slowed down by the collisions occurring inside the other detectors that

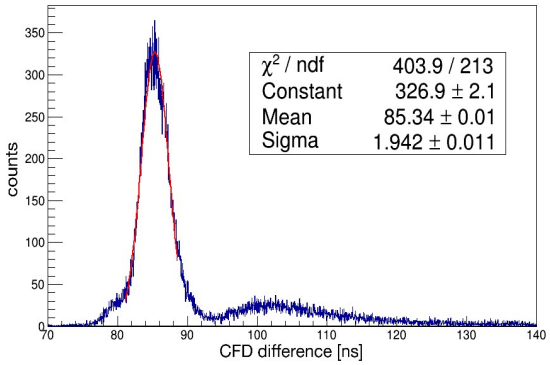

(a) Gaussian fit of the CFD difference between NeutronWall and ΔE traces of channels 6-12

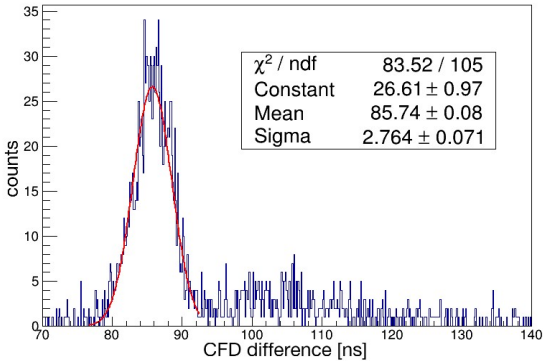

(b) Gaussian fit of the CFD difference between NeutronWall and ΔE traces of low energy of channels 6-12

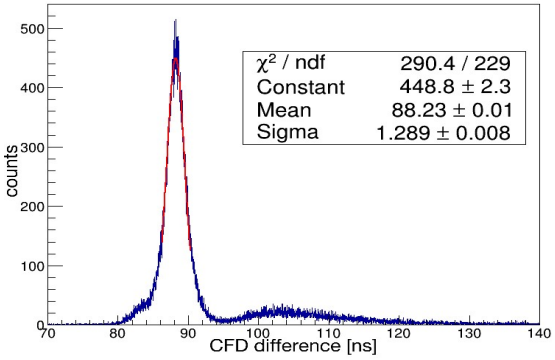

(c) Gaussian fit of the CFD difference between NeutronWall and ΔE traces of channels 6-8

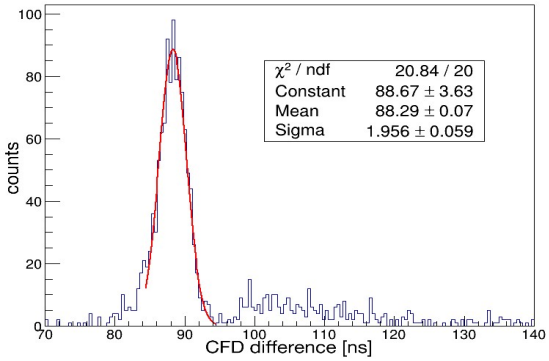

(d) Gaussian fit of the CFD difference between NeutronWall and ΔE traces of low energy of channels 6-8

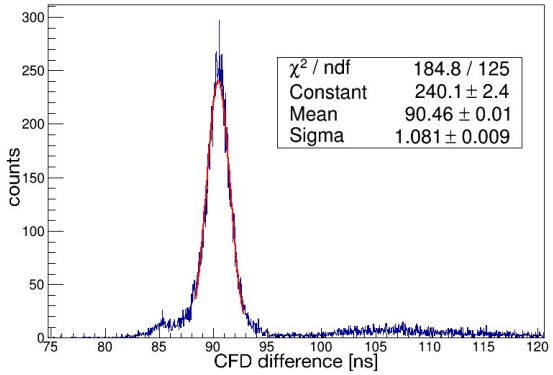

(e) Gaussian fit of the CFD difference between NeutronWall and ΔE traces of channels 6-2

Figure 18: Gaussian fit of the CFD difference between NeutronWall and ΔE traces with and without conditions on energy

Table 7: Time resolution between Neutron Wall and ΔE layers using CFD parameters from table 5

	ch. 6-2	ch. 6-8	ch.6-12
FWHM (ns) without conditions	2.55±0.02	3.04±0.02	4.72±0.03
rel. err.	0.7%	0.7%	0.6%
FWHM (ns) with conditions	—	4.6±0.1	6.5±0.2
rel. err.	—	2.2%	3.1%

surround the target, this is in accord with the experimental results. Notice also that the ToF distribution is quite large: this explains why the related bumps in the CFD differences shown in Fig. 18 are wide, too.

In order to attain an even better time resolution, it was also attempted to isolate the γ peak in the CFD histogram of the OR signal of Neutron Wall (see Fig. 16) and then evaluate the difference with the ΔE traces: the results did not improve with respect to the the ones reported in table 7. This is understood because, as one can see looking at Fig. 18(b) and 18(d) in particular, the counts were already mainly cooresponding to the CFD difference related to the γ peak.

To conclude, in the best case scenario, the time resolution can be about 4.5 ns. In section 5.2, where the comparison with the simulations will be done, it will be verified if this is sufficient to discriminate the incoming particles.

4.3 Induced signals and coincidences

During the experiment, the presence of very low both positive and negative traces was noticed and they were attributed to induced signals in those channels, due to the passage of a particle in one of the other segments.

To better understand the nature and the behavior of these waves, the Scan command of ROOT was used, printing on terminal, for every channel at the same time, the integral under the waveform and the polarity, imposing the passage of one of the identified particles

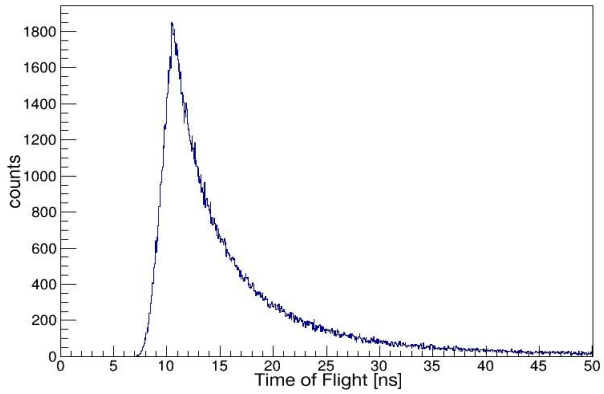

Figure 19: Simulated ToF of neutrons needed to reach the Neutron Wall

in a pair of channels (for example, the response of channels 8-9 and 12-13 to the passage of a proton in channels 2-3): this was done for every particle in each pair of channels.

The principal observation is that the ΔE channels present, in general, more induced signals than the E ones: the reason may be that, since they are thinner, they are more sensitive to small variations in charge distribution caused by ions passing near them, even if not through. Another remarkable fact is that the passage of any particle through channels 2 and 3 cause way more induced signals than the passage of the same type of particle through a pair of the other channels generates in 2 and 3: this may be related to the issue in the electronics of these channels previously supposed. The amplitude of the induced waves is very low with respect to the one of the real particles: referring to Fig. 9, they could be represented by the points composing the structure in the bottom left of the E-ΔE matrices, so values lower than $\sim$20 in ΔE and than $\sim$40 in E in channel units. Lastly, there is no evident correlation between the polarity of the induced signal and the energy or the type of the incident particle, or the channel being crossed, even if, in general, more positive than negative induced signals were observed.

Again with the Scan command on ROOT, a study on the coincidence of particles was made. As expected, most of them involve firstly protons and secondly α, since they constitute the greatest part of the statistic. Even some events involving 3 different segments at the same time were spotted.
The greater part of coincidences occur between channel 9-8 and 3-2, many between 9-8 and 13-12, while only few between 3-2 and 13-12: since an event classified as coincidence can also be the passage of the same isotope through 2 different sectors, this is a direct check of the relative positions of the segments to which the digitizer channels are connected, as shown in Fig. 20.

Figure 20: Scheme of a telescope divided in segments and the respective connected channels

5 Comparisons with the simulations

This section is dedicated to the theoretical check of the results experimentally obtained and the possibilities that they provide for further and in-depth studies.

5.1 Calibration check

The check on the calibration was accomplished by verifying if the origin of the ^{3}He crossing the segments (visible, for example, in Fig. 9(b)) is the elastic scattering of the ^{64}Zn beam with the above-mentioned isotopes implanted inside the W layer.

In order to do that, a simulation of that process was made with the Kinematics Calculator of LISE++, setting the total beam energy at 250 MeV (3.91 MeV/u), supposing that the reaction takes place in the middle of the target and asking for the kinematics plots at the entrance of the detector. The graph in Fig. 21 shows the energy of the scattered nuclei as a function of their angle of emission. For the simulation, the telescope connected to channels 9 and 8 was considered. It was positioned at an angle of $\sim 30^{o}$ with respect to the direction of the beam and it was supposed to be square, having a height and a length of 2 cm each: the green lines represent both the angular and the energetic ranges interested by the detector. As one can see, in that region, the incident ^{3}He particle can acquire an energy included between ~8.77 and ~12.46 MeV/u, that corresponds to

$$\sim 26.31 - 37.38\ MeV.$$

This result has to be compared with the registered energy of the ^{3}He in the experiment, therefore a (E+ΔE)-ΔE matrix was built (because the theoretically calculated energy is the total energy of the particle impinging on the telescope) for channels 9-8 in units of MeV, basing on the conversions reported in table 2. The obtained matrix with the condition on the ^{3}He is depicted on Fig. 22.

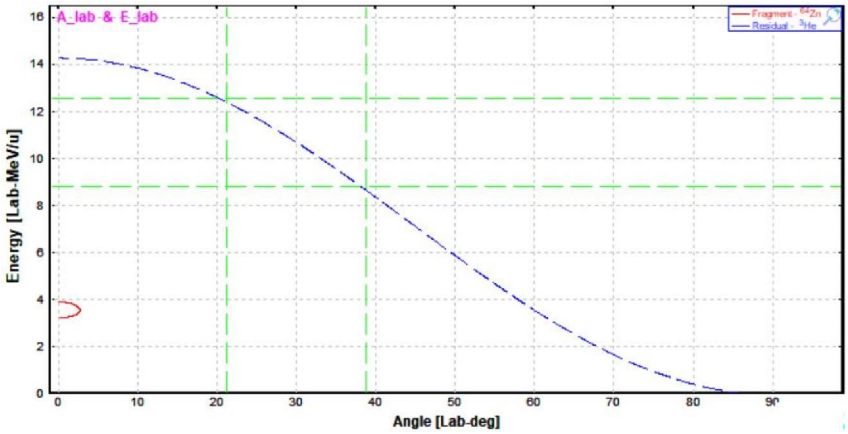

Figure 21: Kinematics plot of the scattering between ^{64}Zn beam and ^{3}He: the range interested by the considered detector is delimited by the green lines

As expected, the number of events is much higher in the energy range predicted for the elastic scattering (~26.31-37.38 MeV), therefore, we are reassured that it actually takes an important part in the ^{3}He statistic and that the calibration was well done.

Since the evaporation of ^{3}He is very unlikey, it is probable that also the low energy events were originated from the scattering between the target and the beam, then slowed down by

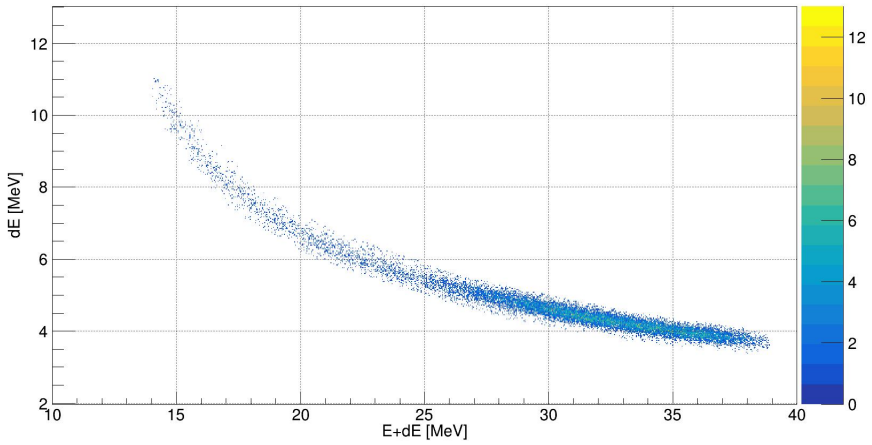

Figure 22: Experimentally registered energy of the ^{3}He by channels 9-8. The greatest part of the events occur in the energy range predicted by the simulations for the elastic scattering between the beam and the target

additional collisions occurring inside the different materials present between the target and the detectors (such as the backing or other sectors of the detector itself).

5.2 Time of Flight

Finally, we wanted to compare the experimental distribution of the charged-particles Time of Flight obtained with the NeutronWall and the ΔE layer with a simulated distribution. Indeed in order to determine if the resolution obtained during the experiment is sufficient to discriminate particles using the ToF, we considered this step as fundamental.

To do that, some Monte Carlo simulations of both the reactions ^{64}Zn $\longrightarrow$ ^{3}He and ^{64}Zn $\longrightarrow$ ^{16}O were accomplished through the COMPA fusion-evaporation reaction code, whose functionalities are described in [6]. In this test, the most realistic situation possible was requested:

- the backing of a ^{179}Au 10mg/cm^2 thickness, with a density of 19.311 g/cm^3, was inserted, as well as the W support, for a thickness of 0.62 μm;
- it was imposed for both p and α to be slowed down by the collisions happening inside the target;
- the ASC (Agata Simulation Code) input was generated to have text files containing the relevant information for the particles.

The output of COMPA is a text file, containing the process simulated event-by-event and includes a number that identifies the evaporated particle, its energy in keV and the direction where it is emitted (expressed in Cartesian coordinates, supposing that the beam hits the target in the origin of the frame of reference). A C++ program was written to convert the output to a ROOT file, containing the energy, the angle of emission (extracted from the direction vector), the velocity of the particle, and the Time of Flight, i.e. the time that the particle needs to cover the distance between the target and the EUCLIDES detector, which is equal to $\sim$6.5 cm. The ToF was evaluated as

$$v = \sqrt{\frac{2E}{m}} \quad \longrightarrow \quad ToF = \frac{d}{v}.$$

The simulations were performed in four different situations:

- ^{3}He target; protons and α detected in the same channel (Fig. 23(a));
- ^{16}O target; protons and α detected in the same channel (Fig. 23(b));
- ^{3}He target; protons and α detected in all possible channels (Fig. 23(c));
- ^{16}O target; protons and α detected in all possible channels (Fig. 23(d)).

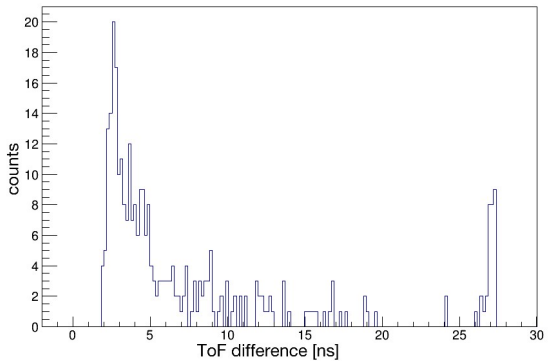

(a) Time of Flight differences between α-particles and protons, setting the ^{3}He target; protons and α detected in the same channel

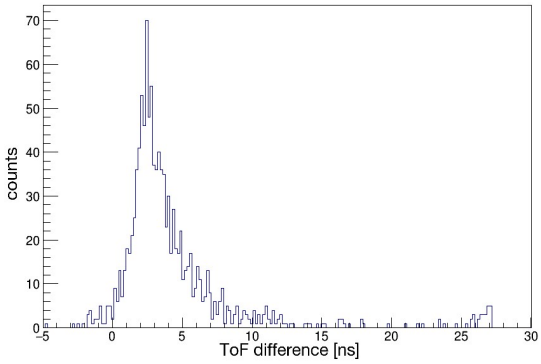

(b) Time of Flight differences between α-particles and protons, setting the ^{16}O target; protons and α detected in the same channel

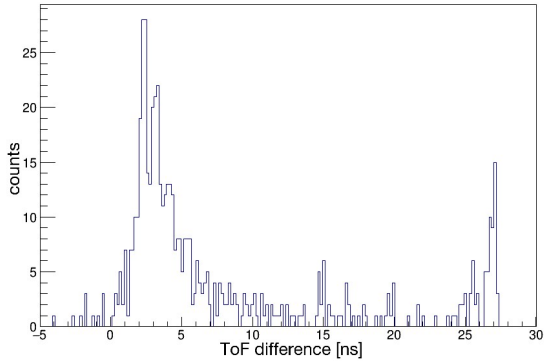

(c) Time of Flight differences between α-particles and protons, setting the ^{3}He target; protons and α detected in all possible channels

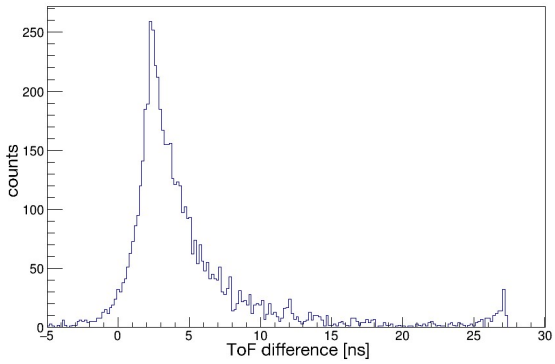

(d) Time of Flight differences between α-particles and protons, setting the ^{16}O target; protons and α detected in all possible channels

Figure 23: Simulation of Time of Flight differences between α-particles and protons in different cases

In Fig. 23, the Time of Flight differences between α and p are reported, setting a condition on energy so that it would have been relevant to discriminate the particles stopping in the ΔE layer (i.e. 3.72 MeV, which is the maximum energy allowed for protons, as said in table 1) and a condition on the difference of angular emission between the two, which was set to 5^{o}, in order to avoid to get the ToF difference between a forward and a backward particle.

Accordingly to the energy distribution of the particles, the majority of the events have a ToF difference of $\sim$2-3 ns. This is an unfortunate result, because the attained time resolution,

as reported in table 7, is of the same order of magnitude, therefore in most cases it would be impossible to distinguish the incoming particles among them.

Nevertheless, a plot of the superposition of the Time of Flight distribution of protons (blue) and α particles (red) having an energy inferior to 3.72 MeV when impinging on the telescope, shows that one can still extract information on the incident particles basing on the Time of Flight, see Fig. 24. Looking at the tails of the histograms, in fact, we deduce that a particle with a ToF greater than $\sim$15 ns must be an α: this also explain the peaks around 27 ns in Fig. 23, which correspond to the difference between very low energy α and $\sim$3.72 MeV protons. Moreover, the fact that, at 3.72 MeV, a proton needs $\sim$2.4 ns to reach the detector, while an α requires $\sim$5 ns, suggests that, even if the ToF difference is about the time resolution, so individually it does not allow to separate the isotopes, a simultaneous and combined analysis of the Time of Flight and the energy could permit to attain the desired results in future studies.

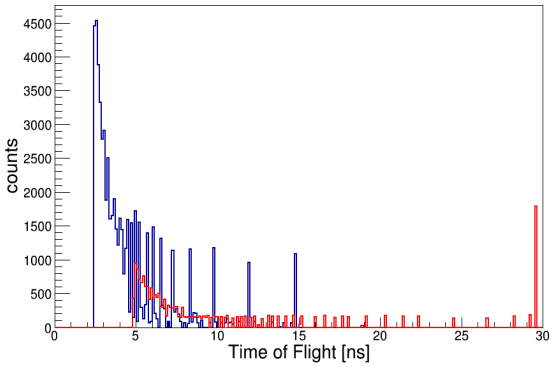

(a) Superposition of the Time of Flight distributions of p and α with ^{3}He target

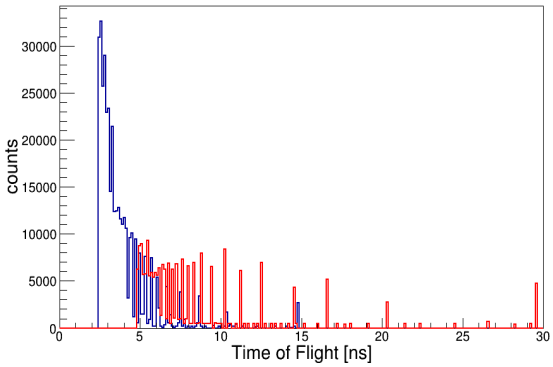

(b) Superposition of the Time of Flight distributions of p and α with ^{16}O target

Figure 24: Simulation of Time of Flight of α particles (red) and protons (blue), both impinging on the telescope having an energy inferior to 4 MeV

6 Conclusions

In this work, the capabilities of a Si E-ΔE telescope of the light charged-particle detector EUCLIDES, coupled with the CAEN V1730B 500 MS/s digitizer, were explored. The main analysed features of this setup are the energy and the timing performances.

The trapezoidal filter technique was used to stimate the energy, using specifically found parameters:

$$k = 285\ samples, \quad l = 500\ samples, \quad k' = 5\ samples.$$

This lead to excellent results, in particular for the segments connected to the channels 8 and 9. In fact, it has been possible to draw some very precise E-ΔE matrices, showing the punch-through of different isotopes. This allowed to calibrate in energy every channel separately. The resulting calibration has finally been verified in section 5.1, where the origin of the ^{3}He events and their energy were investigated.

Also the timing has given excellent outcomes: the accurate search for the CFD parameters lead to separate the cases of high energy and low energy particles, resulting in the time resolutions, between the E and the ΔE layers :

$$FWHM_{high\,energy} = 1.340 \pm 0.003\ ns \qquad FWHM_{low\,energy} = 4.52 \pm 0.01\ ns$$

The CFD difference between the Neutron Wall and the ΔE channels has also been evaluated, since it can be used to determine the time resolution for particles stopped in that silicon layer. In order to do this, restrictions on the energy range of the incident isotopes were set, so that it was important to be able to discriminate, in particular, α particles from protons. The time resolution obtained under these conditions is:

$$FWHM_{stopping\,particles} = 4.6 \pm 0.1\ ns$$

The simulations of the experiment made with COMPA have shown that the Time of Flight difference between α and protons, having both an energy lower than ∼4 MeV, is most likely around 2-3 ns. Therefore, with this time resolution it is not possible to distinguish the incoming particles among them, at least with this particular reaction and with these energies involved.

To conclude, the pulse shape analysis of the outputs of the CAEN V1730B 500 MS/s digitizer connected to a segmented telescope of EUCLIDES has allowed to reach some promising results, that can represent a solid base for the future broadening of this technology to the full structure of the detector and for more detailed studies, such as a disentanglement based not solely on the Time of Flight, but also combined with the energy of the particles involved.

Finally, note that, on this work, a brief article [7], reported in this document as attachment, has also been written and submitted for publication in the Annual Report 2017 of LNL.

7 References

[1] D. Testov et al., *The first physical campaign of the EUCLIDES Si-ball detector coupled to GALILEO gamma-ray spectrometer*, LNL-INFN Ann. Rep. 2015.

[2] D. Testov et al., *Light charged particle detector EUCLIDES for the GALILEO campaign*, LNL-INFN Ann. Rep. 2014.

[3] G. F. Knoll, *Radiation Detection and Measurements*, 4^{th} Edition, John Wiley & Sons Inc, 2010.

[4] C. Tintori, *Digital Pulse Processing in Nuclear Physics*, Rev. 2.1, 2011, from http://www.caen.it/documents/News/20/WP2081_DigitalPulseProcessing_Rev_2.1.pdf.

[5] V. T. Jordanov et al., *Digital synthesis of the pulse shapes in real time for high resolution radiation spectroscopy*, NIM, A 353 (1994) 261.

[6] J. Mierzejewski et al., *The COMPA manual*, from www.old.slcj.uw.edu.pl/∼jmierz/compa.pdf.

[7] G. Sighinolfi et al., *Pulse Shape Analysis of the digitized EUCLIDES signals*, LNL-INFN Ann. Rep. 2017.

Pulse Shape Analysis of the digitized EUCLIDES signals

G. Sighinolfi[1], A. Goasduff[1,2], D. Mengoni[1,2], M. De Rizzo[1], D. Testov[1,2], M. Siciliano[3], G. Jaworski[3], J.J. Valiente-Dobón[3]

[1] *Dipartimento di Fisica e Atronomia dell'Università di Padova, Padova, Italy.*
[2] *INFN, Sezione di Padova, Padova, Italy.*
[3] *INFN, Laboratori Nazionali di Legnaro, Legnaro (Padova), Italy.*

INTRODUCTION

EUCLIDES [1] is a silicon-ball detector of light charged particles, used as an ancillary device of the γ-ray spectrometer GALILEO at LNL [2]. It consists of 55 ΔE-E telescopes of hexagonal and pentagonal shapes, whose thicknesses are ∼130 and ∼1000 μm for ΔE and E layers, respectively, and whose surfaces are ∼10 cm^2 each. The complete structure has a diameter of nearly 13 cm and a solid angle coverage close to 4π. Due to the kinematics enlargement of the solid angle in the center of mass reference frame for a typical fusion-evaporation reaction (v/c≈5%), the most forward positioned telescopes have to deal with higher counting rates with respect to the others. Thus the 5 most forward detectors are segmented in 4 equal parts, which have individual electronic processing circuits, to reduce the probability of pile-up.

In December 2017, the EUCLIDES array was used in an experiment, during which a 250 MeV ^{64}Zn beam was impinging on a ^{3}He target, implanted in a W layer deposited on a thick Au backing. A CAEN V1730B, which is a 1-unit wide VME module housing 16 channels 14-bit 500 MS/s Flash ADC Waveform digitizer, was employed to readout 3 segments of one of the most forward telescopes. 3 even channels were connected to the ΔE layers and 3 odd ones to the E. An additional channel was connected to the OR signal of the Neutron Wall array [3].

The aim of the implementation of this device in the read-out chain of EUCLIDES is to have the possibility to disentangle α and protons stopping in the ΔE layer. Depending on the kinematics of the reaction and the thickness of the absorber layers, used to prevent the elastic scattering of the beam (target) from reaching the detectors, those events stopping in the ΔE can represent more than 50% of the detected particles. In order to reach the maximum particle detection efficiency and selectivity in the light charged particle-γ-rays in fusion-evaporation reaction, new methods of particle discrimination have been investigated for the EUCLIDES array.

EXPERIMENTAL RESULTS

An example of the traces as recorded online by the digitizer during the experiment is presented in Fig. 1. The vertical lines close to 1.25 and 1.5 μs correspond to the OR trigger coming from the Neutron Wall array, which, in this experiment, presents the advantage of being a high efficiency γ-ray detector with a fast response. Due to the large counting rate on this channel (∼ 400 kHz), the choice was made to use it only in coincidence with the E and ΔE signals. The polarity of the waveforms was set negative in the digitizer options and the leading edge threshold was adjusted individually for each channel. As expected, the amplitude of the signals coming from odd channels is larger than the one of even channels, since the first are connected to E segments, in which the energy loss is higher.

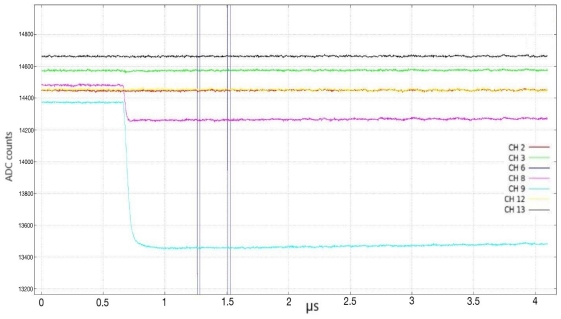

Fig. 1. Online digitized signals from the EUCLIDES segmented detectors read with the CAEN V1730B module during an in-beam experiment. The OR trigger of Neutron Wall and the waveforms of a ΔE and a E channels are visible.

An offline analysis was performed on the digitized signals in order to extract the energy in both E and ΔE layers. Combining the two, the E-ΔE identification matrix, see Fig. 2, was contructed. One can clearly idetify p, d, ^{3}He and α, with some additional structures attributable to t and 2p (or pile-up of protons). Thanks to the clear punch-through of p, d and α, the energy calibrations of the two layers were evaluated. The energies have been extracted by applying a trapezoidal filter following the equations established by Jordanov et al. in [4] on all the traces overcoming a software threshold. This second threshold has been implemented to reduce the processing time, because the CAEN digitizer is sampling all the active channels and dumping them to disk as soon as one of them is overcoming the hardware trigger threshold.

To identify the particles stopping in the ΔE layer, we explore, in this contribution, the discrimination based solely

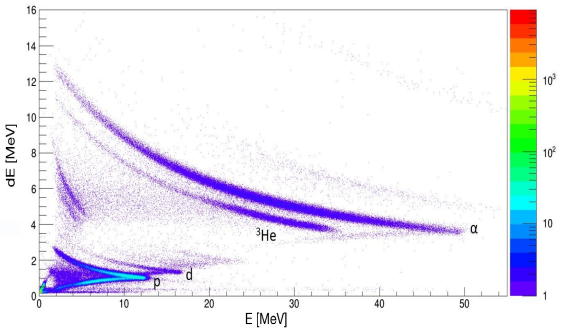

Fig. 2. The E-ΔE matrix obtained after the trapezoidal filtering of the recorded traces for one telescope. The amplitude of the signal extracted in both layers has been calibrated using the punch-through of the light particles.

on the time-of-flight (ToF). Thus a large effort has been dedicated in the optimization of the time resolution based on the difference between two CFD signals. During a preliminary test, the timing performances of the digitizer have been studied through the measurement of the CFD difference between a ∼1 V signal coming from a waveform generator and the same delayed by 16 ns. In this case, an accurate search of the optimal CFD parameters has been achieved through the trial of many different combinations of fraction and delay, looking for the ones giving the lowest possible value of σ for the gaussian fit of the CFD difference between the two. With fraction of 42% and delay of 58 samples, the reached result is FWHM = 50.4±0.2 ps.

Considering the experimental data, the best resolution was obtained with two distinct sets of parameters for the analysis: one for high energy particles, which require smaller values of fraction and delay, and the other for particles at low energy, which need higher ones to overcome the CFD threshold. The first set of parameters leads to a time resolution of ∼1.3 ns between the moment in which the particle hits the ΔE layer and when it hits the E one, while, using the other set, one can get a time resolution of ∼4.5 ns.

To evaluate the ToF of particles stopping in the ΔE layer, the logical OR signal of the Neutron Wall was employed. Since a logical signal was used, it should give a very accurate CFD position and provide a precise time resolution when doing the difference with the CFD of the ΔE traces of the other channels. Setting conditions in order to select only the particles that stop in the first layer and have an energy inferior to 4 MeV, the time resolution is 4.6±0.1 ns, see Fig. 3. Notice that the structure of these CFD differences presents a sharp peak, related to the γ-rays signals in Neutron Wall, followed by a smaller bump, which is instead due to the detection of neutrons.

To understand if this time resolution is sufficient to have the possibility to distinguish α particles from protons stopping in the ΔE layer, a numerical test was made with the COMPA fusion-evaporation reaction code [5], simulating the experiment of interest. The result shows that the ToF difference between α and p to cover the distance separating the detector from the target, at a low enough energy to avoid the punch-through of ΔE, is most likely between 2 and 3 ns. It means that the ToF is too small to allow the particles discrimination based only on the method explained above, at least with this specific reaction and these energies involved. Possible improvements may be obtained through a combined analysis of the ToF and the energy.

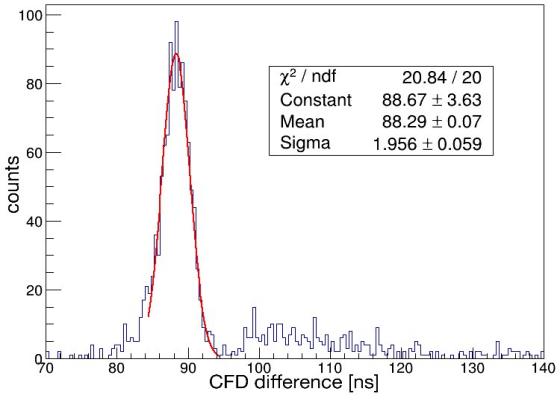

Fig. 3. Time resolution based on digital CFD algorithm applied on Neutron Wall's OR signals and ΔE traces.

CONCLUSIONS

The first experimental results of the implementation of a 500 MS/s digitizer in the read-out chain of an EUCLIDES segmented detector are reported. The offline Pulse Shape analysis provides promising results: the E-ΔE matrix, obtainable through trapezoidal filter, shows a clear identification of the different isotopes; a good time resolution of ∼1.3-4.5 ns between the E and ΔE layer has been obtained. On the other hand, a discrimination based solely on the ToF does not permit to distinguish α particles from protons stopping in the first layer of the detector, at least in this particular experiment: the time resolution of the CFD difference between the Neutron Wall and the ΔE traces of interested particles (esteemed to be ∼4.5 ns) is of the same order of magnitude as the ToF difference between these particles in the previously described experimental conditions (∼2-3 ns).

[1] D. Testov et al., LNL-INFN Ann. Rep. (2015), 105 .
[2] J.J. Valiente-Dobón et al., LNL-INFN Ann. Rep. (2014), 95 .
[3] Ö. Skeppstedt et al., NIM, A 421 (1999), 531.
[4] V. T. Jordanov et al., NIM, A 353 (1994) 261.
[5] J. Mierzejewski et al., *The COMPA manual*, from www.old.slcj.uw.edu.pl/∼jmierz/compa.pdf.